Monthly Notices of the ROYAL ASTRONOMICAL SOCIETY

MNRAS **499,** 3650–3659 (2020) doi:10.1093/mnras/staa3065
Advance Access publication 2020 October 10

An eccentric wave in the circumstellar disc of the Be/X-ray binary X Persei

R. K. Zamanov [1]★ K. A. Stoyanov,[1] U. Wolter,[2] D. Marchev [3] N. A. Tomov,[1] M. F. Bode,[4,5] Y. M. Nikolov,[1] V. Marchev,[1] L. Iliev[1] and I. K. Stateva[1]

[1]*Institute of Astronomy and National Astronomical Observatory, Bulgarian Academy of Sciences, 72 Tsarigradsko Shose, 1784 Sofia, Bulgaria*
[2]*Hamburger Sternwarte, Universität Hamburg, Gojenbergsweg 112, D-21029 Hamburg, Germany*
[3]*Department of Physics and Astronomy, Shumen University, 115 Universitetska Str., 9700 Shumen, Bulgaria*
[4]*Astrophysics Research Institute, Liverpool John Moores University, IC2, 149 Brownlow Hill, Liverpool L3 5RF, UK*
[5]*Office of the Vice Chancellor, Botswana International University of Science and Technology, Private Bag 16, Palapye, Botswana*

Accepted 2020 September 30. Received 2020 September 18; in original form 2020 March 16

ABSTRACT

We present spectroscopic observations of the Be/X-ray binary X Per obtained during the period 2017 December–2020 January (MJD 58095–58865). In 2017 December, the Hα, Hβ, and He I 6678 emission lines were symmetric with violet-to-red peak ratio $V/R \approx 1$. During the first part of the period (2017 December–2018 August), the V/R ratio decreased to 0.5 and the asymmetry developed simultaneously in all three lines. In 2018 September, a third component with velocity ≈250 km s^{-1} appeared on the red side of the He I line profile. Later, this component emerged in Hβ, accompanied by the appearance of a red shoulder in Hα. Assuming that it is due to an eccentric wave in the circumstellar disc, we find that the eccentric wave appeared first in the innermost part of the disc, it spreads out with outflowing velocity $v_{\rm wave} \approx 1.1 \pm 0.2$ km s^{-1}, and the eccentricity of the eccentric wave is $e_{\rm wave} \approx 0.29 \pm 0.07$. A detailed understanding of the origin of such eccentricities would have applications to a wide range of systems from planetary rings to AGNs.

Key words: circumstellar matter – stars: emission-line, Be – stars: individual: X Per – stars: winds, outflows – X-rays: binaries.

1 INTRODUCTION

The relatively bright variable star X Persei (HD 24534) is the optical counterpart of the X-ray source 4U 0352+309 (Braes & Miley 1972) and is classified in the Be/X-ray subclass of massive X-ray binary stars (e.g. Negueruela 2007; Reig 2011). It consists of an early-type Be star and a slowly spinning neutron star. The X-ray data revealed a neutron star with spin period ≈836 s, which exhibits quasi-periodic X-ray flares with a period of ∼7 yr (Nakajima et al. 2019). The pulse period shows episodes of spin-up and spin-down (Acuner et al. 2014) which indicates that the neutron star is close to a torque equilibrium and the long pulse period suggests a strong magnetic field (Yatabe et al. 2018). Delgado-Martí et al. (2001) determined the orbital period ∼250 d, orbital eccentricity $e = 0.11$, semimajor axis H = 2.2 AU, and orbital inclination $e = 26^\circ - 33^\circ$.

During the last century, the visual brightness of X Per has varied in the range V = 6.8–6.2 mag. Spectrograms of X Per from 1913 to 2020 show X Per to have bright hydrogen lines that are variable in structure, velocity, and intensity (e.g. Cowley et al. 1972; Telting et al. 1998). The primary is a rapidly rotating main-sequence Be star that forms an outwardly diffusing gaseous disc. It has projected rotational velocity ≈215 km s^{-1} (Lyubimkov et al. 1997), and is classified as O9.5 (Fabregat et al. 1992), B0Ve (Roche et al. 1997), B1Ve (Zamanov et al. 2019).

In recent decades, X Per exhibited two disc-loss episodes (around 1977 and around 1989) when the emission lines and the circumstellar disc were missing (Roche et al. 1997; Clark et al. 2001). The long-term variability of the emission lines and optical brightness indicate variable mass ejections from the donor star into the circumstellar disc (Li et al. 2014).

We present optical spectroscopic observations obtained in the last two years and discuss asymmetries in the circumstellar disc and the appearance of eccentric wave.

2 OBSERVATIONS

We have 101 optical spectra of X Per on 57 nights secured with the ESpeRo Echelle spectrograph (Bonev et al. 2017) on the 2.0-m RCC telescope of the Rozhen National Astronomical Observatory, Bulgaria, and with the HEROS spectrograph (Schmitt et al. 2014) on the 1.2-m TIGRE telescope in the astronomical observatory La Luz in Mexico. The variability of Hα, Hβ, and He I 6678 emission lines of X Per is presented in Fig. 1. The spectra are normalized to the local continuum and a constant is added to each spectrum. In this figure are plotted only 15 out of 101 spectra obtained.

On the spectra, we measure the following parameters: equivalent width of the line, radial velocities of the peaks, and intensity of the peaks. To measure the radial velocity, we applied Gaussian fitting at the top of the peak. On a few spectra, we see three peaks – one violet and two red peaks. In such cases, we use the stronger red peak to calculate the distance between the peaks and H/E ratio. The measurements are given in a few tables in the Appendix.

3 RESULTS

During the period 2017 December–2020 January, the equivalent width of the Hα emission line (Iα) varies in the range -26 Å $\leq$

★ E-mail: rkz@astro.bas.bg

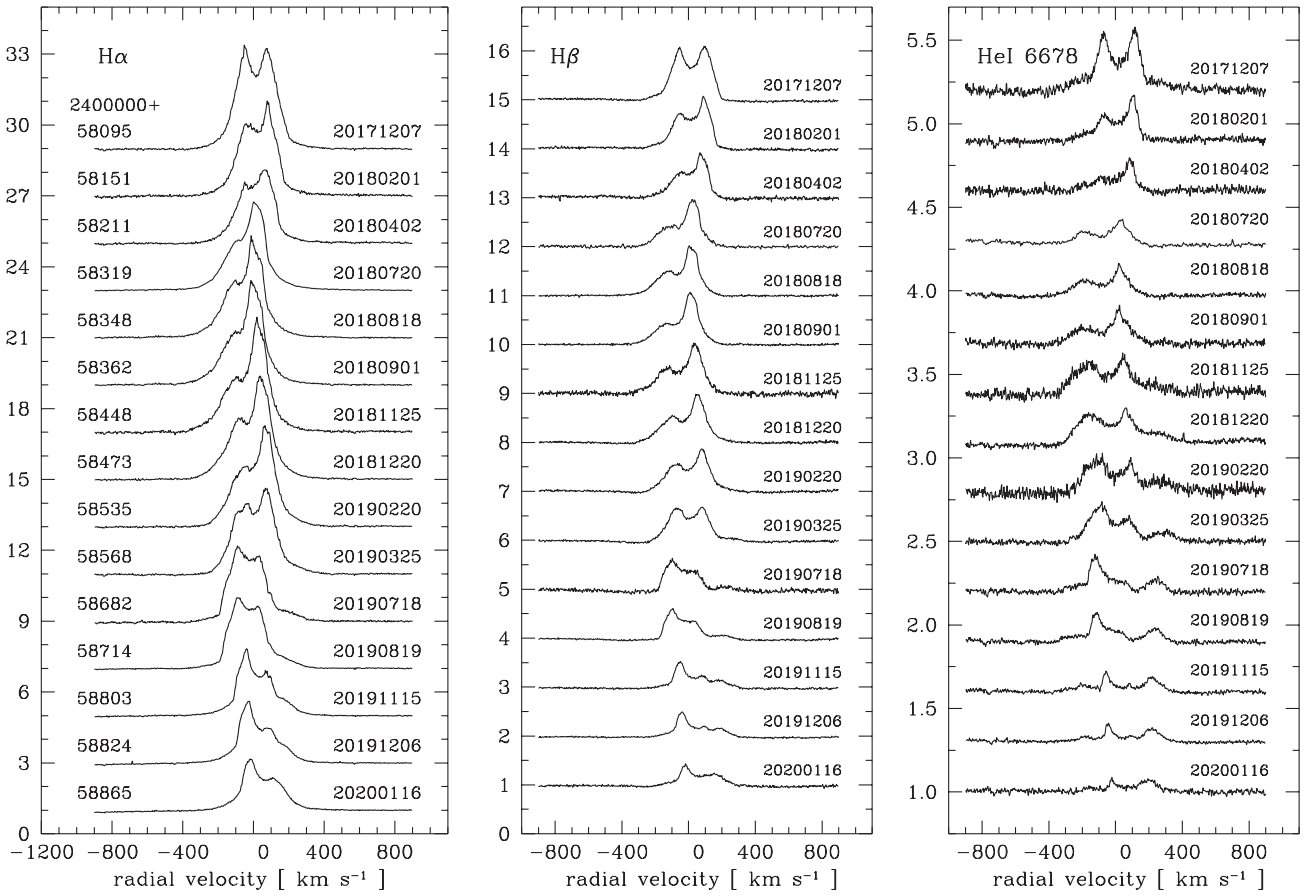

Figure 1. Variability of H α, H β, and He I 6678 emission-line profiles of X Per. The date of observations is in the format YYYYMMDD.

$W\alpha \leq -10$ Å, the equivalent width of the H β emission line (H β) varies in the range -4.4 Å $\leq$ E$\beta \leq -1.4$ Å, and the equivalent width of the He I 6678 emission line varies in the range $-2.0 \leq W$(He I 6678) ≤ -0.4 Å. The variability of the equivalent widths is presented in Fig. 2, together with *V*-band magnitude and X-ray flux in 2–10 keV. The *V*-band data are from the American Association of Variable Star Observers (AAVSO). The X-ray data are from MAXI (Matsuoka et al. 2009). The vertical dashed lines indicate the three periods discussed in Section 3.2. There is a correlation between equivalent widths of these three lines. The correlation analysis between $W\alpha$ and $W\beta$, $W\alpha - W$(He I6678), $W\beta - W$(He I 6678) gives correlation coefficient $\geq$0.80, significance *p*-value $< 10^{-15}$, in other words, a very strong correlation between the equivalent widths of the three lines.

It can be seen from Fig. 2 that when the $W\alpha$ decreases, the *V*-band brightness of X Per increases. The connection between H α and *V*-band magnitude might be caused by the mass ejection from the Be star as discussed in section 4.1 by Li et al. (2014). There are no large changes in the X-ray flux. This indicates that the variability of the emission lines during the period 2017 December–2020 January does not affect the mass accretion rate on to the neutron star.

3.1 Disc size

The variability of the distance between the peaks is presented in Fig. 3. The emission lines form in the disc surrounding the Be star. The discs of the Be stars are Keplerian supported by the rotation (e.g. Rivinius, Carciofi & Martayan 2013; 2016, and references

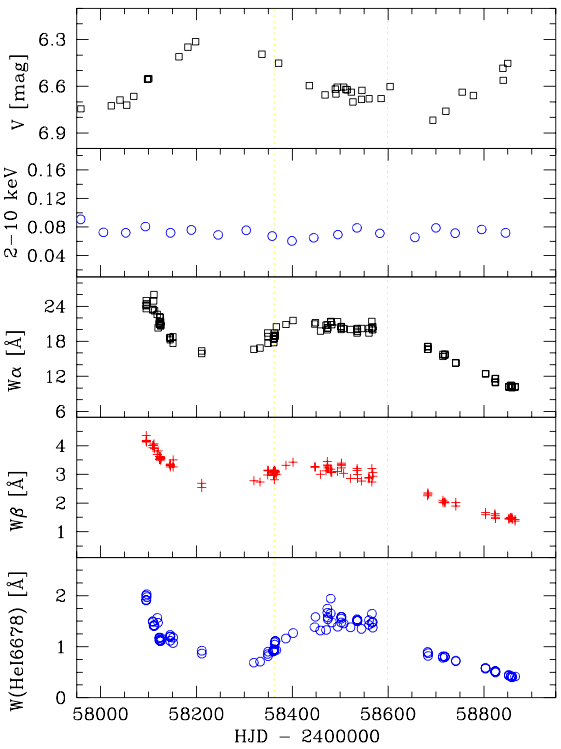

Figure 2. Variability of X Per in *V* band (AAVSO), 2–10 keV X-rays (MAXI), and the equivalent widths of the emission lines H α (black squares), H β (red pluses), and He I 6678 (blue circles).

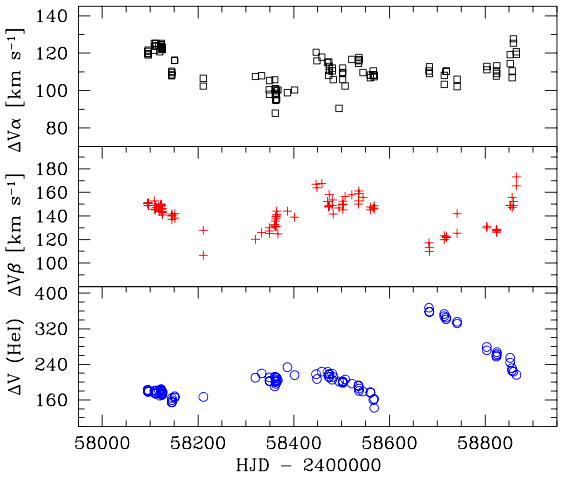

Figure 3. The distance between the peaks of the emission lines – H α (black squares), H β (red pluses), and He I 6678 (blue circles).

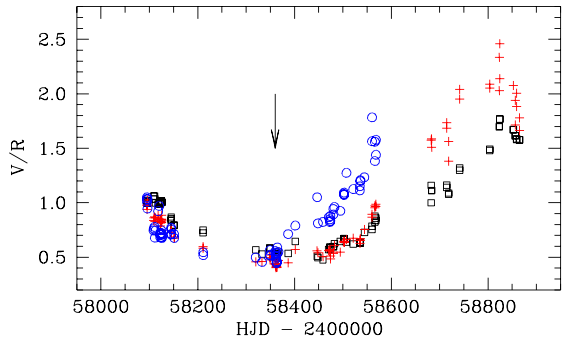

Figure 4. V/R ratio for H α (black squares), H β (red pluses), and He I 6678 (blue circles). The arrow indicates the appearance of the eccentric wave.

therein]. For a Keplerian circumstellar disc, the peak separation can be regarded as a measure of the outer radius ($R_{\rm disc}$) of the emitting disc (Huang 1972):

$$R_{\rm disc} = R_1 \frac{(2\,v\,\sin i)^2}{\Delta V^2}, \quad (1)$$

where R_1 is the radius of the primary and $v \sin i$ is its projected rotational velocity. Radii estimation through this method is a good approximation for symmetric profiles. The projected rotational velocity of the primary is estimated to be $v \sin i = 200$ km s^{-1} (Slettebak 1982), $v \sin i = 215 \pm 10$ km s^{-1} using the He I λ4026-Å absorption line (Lyubimkov et al. 1997) and $v \sin i = 191 \pm 12$ km s^{-1} from the width of the H α emission (Zamanov et al. 2019). For the primary, we adopt $R_1 = 10.5\,R_\odot$ and mass $M_1 = 13.5\,M_\odot$ (Zamanov et al. 2019). This gives the Keplerian velocity on the surface of the star $V_{\rm Kepl} = 495$ km s^{-1}. Adopting inclination $i = 30^\circ$ (Delgado-Martí et al. 2001), and that the star rotates with 0.8 of the critical velocity (e.g. Porter & Rivinius 2003), we estimate $v \sin i \approx 198$ km s^{-1}, which is in agreement with the above values. This agreement also is a clue that there is no considerable deviation between the orbital plane of the binary and the equatorial plane of the Be star. If it exists at all it should be less then 5°.

On the spectrum 20190325 (see Fig. 1), the He I emission extends up to ≈370 km s^{-1} at zero intensity. We note that velocities in the profiles of the emission lines >495sin i km s^{-1}, which is ≈250 km s^{-1}, are probably super-Keplerian velocities, and indicate eccentric motion in the disc, where these parts of the emission line are formed (see Section 3.3).

In 2017 December, the emission lines have double-peaked symmetric profiles (see Fig. 1). For five spectra obtained in 2017 December, we measure $\Delta V\alpha = 120 \pm 1$ km s^{-1}, $\Delta V\beta = 150 \pm 1$ km s^{-1}, and $\Delta V_{\rm He\,I} = 180 \pm 2$ km s^{-1}. Using equation (1), these values correspond to disc size $R_{\rm disc}$(H α) = 134 $R_\odot$, $R_{\rm disc}$(H β) = 86 $R_\odot$, and $R_{\rm disc}$(He I 6678) = 60 $R_\odot$. During the period of our observations, the average distance between the peaks of the lines is $\Delta V\alpha = 111 \pm 14$ km s^{-1}, $\Delta V\beta = 142 \pm 13$ km s^{-1}, and $\Delta V_{\rm He\,I} = 213 \pm 52$ km s^{-1}. These values correspond to the following average disc size for different emission lines (calculated using equation 1): $R_{\rm disc}$(H α) = 156 $R_\odot$, $R_{\rm disc}$(H β) = 96 $R_\odot$, $R_{\rm disc}$(He I 6678) = 43 $R_\odot$. The typical errors are about ± 5 per cent. For the calculations of the outflowing velocity (Section 4.1), we will use $R_{\rm disc}$(H β) = 86–96 $R_\odot$. The average ratios between disc sizes (which is equivalent to the ratio of the peak separations) are $R_{\rm disc}$(H α)/$R_{\rm disc}$(H β) = 1.62 and $R_{\rm disc}$(H α)/$R_{\rm disc}$(He I 6678) = 3.63.

3.2 *V/R* ratio and asymmetries in the disc

In Fig. 1, it is seen that the emission lines are symmetric in 2017 December, with *V/R* ratio ≈1. After that, all three lines become asymmetric. Fig. 4 presents the *V/R* ratio, calculated as $V/R = (I_V - 1)/(I_R - 1)$, where I_V and I_R are the intensity of the blue (violet) and red peak, respectively. The spectra are normalized before the measurements and the continuum level is ≡ 1.0.

(1) During the first part of the period (MJD 58095–58365) in all three lines the *V/R* ratio varies in practically the same manner – it decreased from *V/R* ≈ 1 to *V/R* ≈ 0.5, with speed $\Delta(V/R)/\Delta t \approx 2 \times 10^{-3}$ d^{-1}. The fact that the changes in *V/R* ratio are practically identical in all three lines (H α, H β, and He I; see Fig. 4) means that the asymmetry develops in the entire disc simultaneously.

(2) During the second part of the period (MJD 58365–58600), the *V/R* ratio of H α and H β goes up from 0.5 to ∼1.0. However the behaviour of the *V/R* ratio of He I 6678 deviates from the behaviour of the H α and H β lines (see Fig. 4). *V/R* (He I) changes from 0.5 to 1.5, having a faster rate of change $\Delta(V/R)/\Delta t \approx 4 \times 10^{-3}$ d^{-1}. For comparison, the H α emission peaks have rate of change $\Delta(V/R)/\Delta t \approx 1.7 \times 10^{-3}$ d^{-1} and the H β peaks – $\Delta(V/R)/\Delta t \approx 2.3 \times 10^{-3}$ d^{-1} . In addition to that, a third component appeared in the red side of the He I profile (Fig. 7). This third component emerged in He I in 2018 November. This is an indication that the structural changes begin in the innermost region of the disc.

(3) The behaviour of the *V/R* ratio of H β is similar to that of H α till MJD 58600. After that, it begins to deviate (see Fig. 4). This is an indication that the asymmetry spreads out in the disc.

The development of asymmetries visible in the H α peaks corresponds to processes in the outer parts, while the variability of He I is connected with changes in the inner parts of the circumstellar disc.

3.3 Third component in He I

In 2018 November, a third component appears in the red side of the He I line. In 2019 March, this component peaks at radial velocity ∼250 km s^{-1}, and at zero intensity, it is in the range 130–390 km s^{-1}. The three-component structure is demonstrated on Fig. 7, left-hand panel. The Keplerian velocity around the primary is $V_{\rm Kepl} = \sqrt{GM_1/r}$, where I is the gravitational constant and r is the distance. We estimate that the observed velocity of the third component corresponds to a distance from the centre of the primary

of 40–20 $R_\odot$, respectively. Bearing in mind that $R_1 \approx 10.5\,R_\odot$, it means that this component originates somewhere about 1–3 stellar radii above the stellar surface. The velocity of this component is similar to the velocities observed during the double disc formation in 1994 (Tarasov & Roche 1995), when the blue and red peaks of the inner disc were at −308 and +258 km s^{-1}, respectively.

4 ECCENTRIC WAVE

The discs around stars, or other central massive bodies, can support disturbances in which the fluid motion is nearly Keplerian with non-zero eccentricity. The eccentric waves are expected not only in Be discs but also in accretion discs, protoplanetary discs, and in discs with an embedded planet (e.g. Lynch & Ogilvie (2019) and references therein). In X Per, the appearance of a significant density enhancement in the disc near the stellar surface and its evolution was also observed and discussed by Tarasov & Roche (1995) and Clark et al. (2001). Assuming that the observed behaviour of the emission lines of X Per is due to an eccentric wave, we calculate its velocity and eccentricity.

4.1 Velocity of the eccentric wave

We first see the appearance of the third component in He I lines on our spectrum in 2018 November (20181124). It is not visible on our spectrum obtained in 2018 mid-October (20181010). In 2019 March, this component starts to be visible in the red side of H β. The profile of H β on 2019 December 5 (20191205) with three peaks is similar to that of He I obtained eight months earlier (20190325); see Fig. 7. We suppose that the eccentric wave began somewhere about MJD 58360 (about the end of 2018 August) when the behaviour of the He I peaks started to deviate from H β and H α (see the arrow on Fig. 4). At this time, it is likely to be at a distance H $\geq$ E$_1$. It reached near the outer edge of the H β disc in 2020 January (when the two red peaks of H β blended). This indicates that the eccentric wave spreads from inside out. Bearing in mind the disc size in the lines (Section 3.1), this corresponds to an outflowing velocity of the wave, $v_{\rm wave} \approx 1.2 \pm 0.1$ km s^{-1}.

In the above calculation, we supposed that the motion of the density wave is linear. We also supposed that the peak merging corresponds to the moment when the wave reached the outer edge. We performed numerical experiments with Gaussian fitting of the peaks and their blending (merging). The experiments showed that to observe two peaks, the difference between their velocities must be $\gtrsim$30 km s^{-1}. If it is less than 30 km s^{-1}, then we will see one peak. This value depends on the signal-to-noise ratio of the spectra, width of the peaks, their intensity, etc. This limit of 30 km s^{-1} was found with numerical experiment with two Gaussian peaks, having width and intensity similar to those observed. This also indicates that the above estimation should be considered as an upper limit of $v_{\rm wave}$. Assuming that the merging of the peaks corresponds to the moment when the wave is at 0.85 ± 0.15 of the disc size, this will give $v_{\rm wave} \approx 1.1 \pm 0.2$ km s^{-1}.

In Fig. 5 are plotted the heliocentric radial velocities of the peaks for H α ($V_r\alpha$), H β ($V_r\beta$), and He I 6678 (V_rHe I). The radial velocities of the He I peaks indicate that the wave begins somewhere about MJD 58350 (2018 August). The radial velocities of the H β peaks indicate that the two red peaks merged somewhere about MJD 58850 (2020 January).

In Fig. 6, we plot the distance between the peaks of H α normalized with the stellar rotation versus $W\alpha$. These two parameters correlate in the Be stars, representing the fact that the disc grows as $W\alpha$ increases. The black open circles are data for Be stars taken from Andrillat (1983), Hanuschik (1986), Hanuschik, Kozok & Kaiser (1988), Dachs, Hummel & Hanuschik (1992), Slettebak, Collins & Truax (1992), and Catanzaro (2013). The red plus signs are our measurements of X Per. We see that X Per is close to the average behaviour of the Be stars. This indicates that the eccentric wave does not change the overall structure of the circumstellar disc.

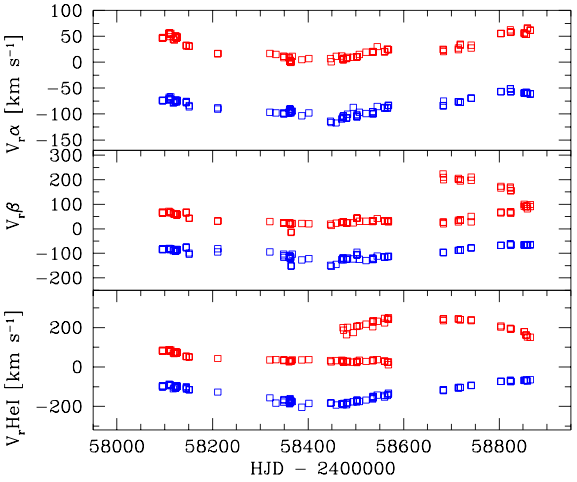

Figure 5. Radial velocities of the peaks.

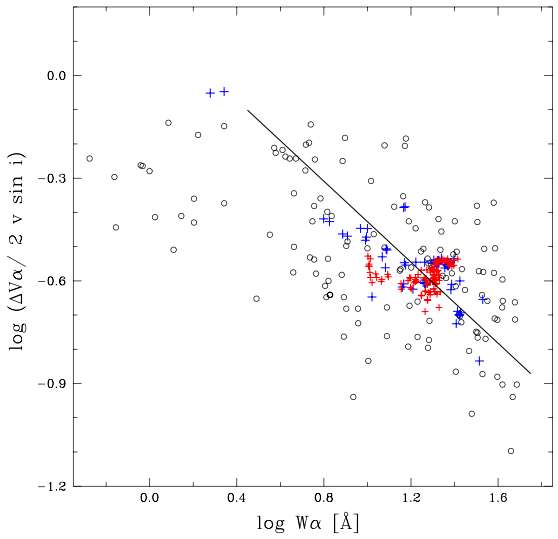

Figure 6. $\Delta V\alpha$ versus $W\alpha$. The circles are the Be stars (see the text) and the red crosses are our observations of X Per.

4.2 Eccentricity of the eccentric wave

The vis-viva equation connects the instantaneous orbital speed of a body at any given point in its trajectory with distance. For periastron and apastron, we have

$$v_{\rm per} = \sqrt{GM_1\left(\frac{2}{a(1-e)} - \frac{1}{a}\right)}, \quad (2)$$

$$v_{\rm ap} = \sqrt{GM_1\left(\frac{2}{a(1+e)} - \frac{1}{a}\right)} \quad (3)$$

Table 1. The date of observations (in the format YYYYMMDD), heliocentric radial velocities of the three peaks, and the calculated eccentricity of the eccentric wave.

Date-obs	V_{r1}	V_{r2}	V_{r3}	$e_{\rm wave}$
He I 6678				
20190221	− 147.2	29.9	231.9	0.17
20190323	− 137.7	24.8	247.8	0.23
20190325	− 133.4	23.9	246.3	0.24
20190220	− 155.1	29.8	249.0	0.18
H β				
20190819	− 89.6	33.0	210.2	0.33
20190822	− 86.6	39.2	201.5	0.32
20191115	− 67.0	62.0	176.2	0.36
20191206	− 65.8	63.6	157.6	0.31
H α				
20191115	− 57.1	59.8	145.2	0.33
20191115	− 56.9	55.0	148.6	0.36
20191206	− 63.5	52.3	155.6	0.32

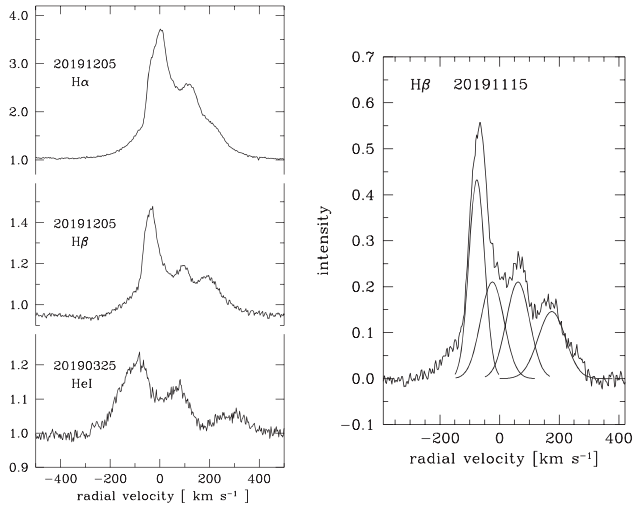

Figure 7. The left panel shows the three component structure of He I 6678 and H β lines, and red shoulder in the H α line. The right panel shows an approximation with four Gaussians (see Section 4.2).

where a is the length of the semimajor axis of the elliptical orbit, and $a(1-e)$ and $a(1+e)$ are the distances at which the speed is to be calculated (in our case, periastron and apastron, respectively).

Using three spectra on which H α is symmetric (20161211, 20170317, 20171207), we measure the velocity at the half-maximum of the H α emission -11 ± 3 km s^{-1}. The measurement is done using the position of the bisector at the half-maximum intensity of the emission, as shown in fig. 1 of Glebocki et al. (1986). The old spectroscopic data of Hutchings (1977) give an average value for the radial velocity of the Balmer absorption ≈ -20 km s^{-1} and for He I lines -19 ± 10 km s^{-1}. Grundstrom et al. (2007) give systemic velocity $\gamma = 1.0 \pm 0.9$ km s^{-1} on the basis of absorption lines in the *IUE* spectra. On the spectra where these peaks are visible, we measure the heliocentric radial velocities of the peaks. They are given in Table 1. For He I and H β, these are measurements of the peaks. For H α, it is the velocity of the shoulder. Correcting these values for the systemic velocity,

$$V_{r1} - \gamma = v_{ap} \sin i$$

and

$$V_{r3} - \gamma = v_{per} \sin i,$$

and using equations (2) and (3), we estimate the eccentricity of the wave, which is given in the last column of Table 1. The average eccentricity of the wave is $e_{\rm wave} = 0.29 \pm 0.07$.

In the above calculations, we adopted $\gamma = -11$ km s^{-1}. If we assume $\gamma = -1$ km s^{-1}, the estimated $e_{\rm wave}$ will increase up to $e_{\rm wave} = 0.36 \pm 0.07$. There should be two blue peaks corresponding to the two red peaks. In our spectra we see only one; see Fig. 7 (left panel). It means that the two blue peaks are blended (and have approximately equal velocities). To estimate the possible influence of the blending on our value of $e_{\rm wave}$, we fitted the profile with four Gaussian (Fig. 7, right panel). During the fitting, we explicitly assumed that the two inner peaks are identical. The fitting suggests that the peak (corresponding to the wave) could be blueshifted with 10–20 km s^{-1}. A correction of -10 km s^{-1} to the measured radial velocity produces a lower value $e_{\rm wave} = 0.24 \pm 0.06$. These two sources of uncertainty give the range $0.16 < e_{\rm wave} < 0.42$ for the eccentricity of the wave.

5 DISCUSSION

Eccentric discs, in which planet, or star, or fluid elements follow elliptical orbits of variable eccentricity around a central mass, have applications in various astrophysical objects: Be stars (Ogilvie 2008), galactic nuclei (Cao et al. 2018), and planetary rings and protoplanetary discs (Lee, Dempsey & Lithwick 2019; Martin, Lissauer & Quarles 2020). A more deep understanding of the appearance and the evolution of asymmetries and eccentricities in the circumstellar disc of X Per and other Be/X-ray binaries would therefore be of general interest. There are different theories about the origin of the long-term variability observed in Be stars (e.g. Hanuschik et al. 1995, section 4.2). The most accepted is the global oscillation scenario, which proposes that a Keplerian disc around a Be stars is subject to global distortion – a one-armed density wave (Okazaki 1991; Savonije & Heemskerk 1993; Papaloizou & Savonije 2006), which is an updated and sophisticated version of the old elliptical disc model (Struve 1931). Eccentric mode in Be/X-ray binaries can be excited in the disc through direct driving as a result of a one-armed bar potential of the binary (Okazaki et al. 2002).

In our opinion, during the first part or our observations (MJD 58 095–58 365) we observe a global distortion (H α, H β, He I vary together) similar to that observed in H 1145−619 (see fig. 7 by Alfonso-Garzón et al. 2017). During the period MJD 58 365–58 865, we observe an eccentric wave, which starts in the innermost parts of the disc and spreads out with velocity $v_{\rm wave} \approx 1.1$ km s^{-1}. Once the wave is in the disc, it should begin to rotate. Its rotation is expected to be much slower than the disc rotation (Okazaki & Kato 1986). The radial velocities on Fig. 5 indicate that the period of rotation of the density wave is probably ∼800 d.

The interesting behaviour of the He I emission of X Per was studied by Kunjaya & Hirata (1995) and Tarasov & Roche (1995). They observed four peaks in He I emission in 1995 and suggested the formation of a double circumstellar disc. Hirata & Kogure (1977) were the first to argue about the existence of a two-component structure of the circumstellar envelope around a Be stars following the example of the well-known star Pleione (BU Tau). They proposed a model consisting of two layers and also considered a separate fast-rotating layer closer to the stellar equator. The formation of a new envelope, coexisting with the previous one is also detected by Nemravová et al. (2010) on the basis of the four-peak structure of H α

emission. Clark et al. (2001) presented an extensive data set of X Per, covering the period 1987–2001, and interpreted the He I variability as a formation of a density wave that moves towards the outer parts faster than the disc formation. It is likely that the four peaks profiles of X Per in 1995 represented a wave with eccentricity almost zero.

Following Delgado-Martí et al. (2001), the periastron passages of the neutron star is expected at

$$\mathrm{MJD}\,51353(\pm7) + 250.3(\pm0.6) \times E.$$

The excitation of the eccentric wave could be connected with the periastron passage at about MJD 58 361. The periastron passage of the neutron star initiates (generates) a higher tidal wave on the stellar surface. Superposition of a high tide with another mechanism (e.g. non-radial pulsations) could cause a mass ejection event from the star surface into the inner disc. A similar mass ejection was already discussed by Li et al. (2014) in connection between the long-term variability of the Hα line and the X-ray emission from the neutron star. The recent radiative transfer calculations on the structure of Be discs in coplanar circular binary systems suggest a *V/R* cycle every half orbital period (Panoglou et al. 2018). We do not see signs of such modulation in X Per in our data, which cover 770 d, i.e. more than three orbital periods.

CONCLUSIONS

We report 100 spectral observations of the Be/X-ray binary X Per during the period December 2017–January 2020. We study the evolution of the profiles of the emission lines Hα, Hβ, and He I 6678, which are formed in the Be circumstellar disc. Their evolution suggests an eccentric wave in the circumstellar disc, for which we find that (1) it spreads from inside out; (2) its velocity is $v_{\rm wave} = 1.1 \pm 0.2$ km s^{-1}; and (3) the eccentricity of the eccentric wave is in the range $0.17 \leq e_{\rm wave} \leq 0.41$.

The development of asymmetries in the inner and outer parts of the circumstellar disc in the Be/X-ray binary X Per provides a laboratory to test the theoretical models of eccentric waves in the Be discs. We encourage high-resolution spectroscopic observations of this relatively bright object (e.g. Echelle spectrographs on 2.0-m class telescopes) to monitor the evolution of the emission lines.

ACKNOWLEDGEMENTS

This work was supported by the Bulgarian National Science Fund project number КП-06-H28/2 08.12.2018 'Binary stars with compact object'. The TIGRE telescope is a collaboration of the Hamburger Sternwarte, the Universities of Hamburg, Guanajuato, and Liége. UW acknowledges funding by DLR, project 50OR1701. DM acknowledges partial support by grant RD-08-122/2020 from Shumen University. This research has made use of the MAXI data provided by RIKEN, JAXA, and the MAXI team and observations from the AAVSO International Database contributed by observers worldwide. We are very grateful to the anonymous referee for the very helpful and constructive comments on the original paper.

DATA AVAILABILITY

The spectra are available upon request from the authors: rkz@astro.bas.bg, kstoyanov@astro.bas.bg.

REFERENCES

Acuner Z., İnam S. Ç., Şahiner Ş., Serim M. M., Baykal A., Baykal J., 2014, MNRAS, 444, 457
Alfonso-Garzón J. et al., 2017, A&A, 607, A52
Andrillat Y., 1983, A&AS, 53, 319
Bonev T. et al., 2017, Bulg. Astron. J., 26, 67
Braes L. L. E., Miley G. K., 1972, Nature, 235, 273
Cao R., Liu F. K., Zhou Z. Q., Komossa S., Ho L. C., 2018, MNRAS, 480, 2929
Catanzaro G., 2013, A&A, 550, A79
Clark J. S., Tarasov A. E., Okazaki A. T., Roche P., Lyuty V. M., 2001, A&A, 380, 615
Cowley A. P., McLaughlin D. B., Toney J., MacConnell D. J., 1972, PASP, 84, 834
Dachs J., Hummel W., Hanuschik R. W., 1992, A&AS, 95, 437
Delgado-Martí H., Levine A. M., Pfahl E., Rappaport S. A., 2001, ApJ, 546, 455
Fabregat J. et al., 1992, A&A, 259, 522
Glebocki R., Sikorski J., Bielicz E., Krogulec M., 1986, A&A, 158 , 392
Grundstrom E. D. et al., 2007, ApJ, 660, 1398
Hanuschik R. W., 1986, A&A, 166, 185
Hanuschik R. W., Hummel W., Dietle O., Sutorius E., 1995, A&A, 300, 163
Hanuschik R. W., Kozok J. R., Kaiser D., 1988, A&A, 189, 147
Hirata R., Kogure T., 1977, PASJ, 29, 477
Huang S.-S., 1972, ApJ, 171, 549
Hutchigs, J. B.,1977, MNRAS, 181, 619
Kunjaya C., Hirata R., 1995, PASJ, 47, 58 9
Lee W.-K., Dempsey A. M., Lithwick Y., 2019, ApJ, 882, L11
Li H., Yan J., Zhou J., Liu Q., 2014, AJ, 148, 113
Lynch E. M., Ogilvie G. I., 2019, MNRAS, 488, 1127
Lyubimkov L. S., Rostopchin S. I., Roche P., Tarasov A. E., 1997, MNRAS, 286, 549
Martin R. G., Lissauer J. J., Quarles B., 2020, MNRAS, 496, 2436
Matsuoka M. et al., 2009, PASJ, 61, 999
Nakajima M., Negoro H., Mihara T., Sugizaki M., Yatabe F., Makishima K., 2019, in Oskinova L. M., Bozzo E., Bulik T., Gies D. R., eds, Proc. IAU Symp. 346, High-mass X-ray Binaries: Illuminating the Passage from Massive Binaries to Merging Compact Objects. Kluwer, Dordrecht, p. 131
Negueruela I., 2007, in St. Louis N., Moffat A. F. J., eds, ASP Conf. Ser. Vol. 367, Massive Stars in Interactive Binaries. Astron. Soc. Pac., San Francisco. p. 477
Nemravová J. et al., 2010, A&A, 516, A80
Ogilvie G. I., 2008, MNRAS, 388, 1372
Okazaki A. T., 1991, PASJ, 43, 75
Okazaki A. T., 2016, in Sigut T. A. A., Jones C. E., eds, ASP Conf. Ser. Vol. 506, Bright Emissaries: Be Stars as Messengers of Star-Disk Physics. Astron. Soc. Pac., San Francisco, p. 3
Okazaki A. T., Bate M. R., Ogilvie G. I., Pringle J. E., 2002, MNRAS, 337, 967
Okazaki A. T., Kato S., 1986, Ap&SS, 119, 109
Panoglou D., Faes D. M., Carciofi A. C., Okazaki A. T., Baade D., Rivinius T., Borges Fernandes M., 2018, MNRAS, 473, 3039
Papaloizou J. C. B., Savonije G. J., 2006, A&A, 456, 1097
Porter J. M., Rivinius T., 2003, PASP, 115, 1153
Reig P., 2011, Ap&SS, 332, 1
Rivinius T., Carciofi A. C., Martayan C., 2013, A&A Rev., 21, 69
Roche P. et al., 1997, A&A, 322, 139
Savonije G. J., Heemskerk M. H. M., 1993, A&A, 276, 409
Schmitt J. H. M. M. et al., 2014, Astron. Nachr., 335, 787
Slettebak A., 1982, ApJS, 50, 55
Slettebak A., Collins G. W. II, Truax R., 1992, ApJS, 81, 335
Struve O., 1931, ApJ, 73, 94
Tarasov A. E., Roche P., 1995, MNRAS, 276, L19
Telting J. H., Waters L. B. F. M., Roche P., Boogert A. C. A., Clark J. S., de Martino D., Persi P., 1998, MNRAS, 296, 785

Yatabe F., Makishima K., Mihara T., Nakajima M., Sugizaki M., Kitamoto S., Yoshida Y., Takagi T., 2018, PASJ, 70, 89
Zamanov R., Stoyanov K. A., Wolter U., Marchev D., Petrov N. I., 2019, A&A, 622, A173

APPENDIX

Journal of observations is given in Table A1. The measurements are summirized in Tables A2– A4.

Table A1. Journal of observations.

Date-obs	Obs.	Exp-time (s)	JD
2015-12-23T23:16	Rozhen	1800	57 380.47 503
2015-12-23T23:48	Rozhen	600	57 380.49672
2015-12-24T20:51	Rozhen	600	57 381.37 398
2015-12-26T20:01	Rozhen	600	57 383.33 892
2015-12-27T20:56	Rozhen	300	57 384.37 750
2016-01-30T19:10	Rozhen	300	57 418.30 099
2016-09-23T01:42	Rozhen	600	57 654.57 407
2016-09-23T01:42	Rozhen	600	57 654.57 407
2016-12-11T20:58	Rozhen	1200	57 734.37 953
2017-03-17T18:58	Rozhen	1200	57 830.28 854
2017-12-07T16:57	Rozhen	120	58 095.21 181
2017-12-07T17:03	Rozhen	900	58 095.21 620
2017-12-07T17:20	Rozhen	900	58 095.22 811
2017-12-08T16:45	Rozhen	120	58 096.20 389
2017-12-08T16:50	Rozhen	600	58 096.20 690
2017-12-21T03:34	'LaLuz'	240	58 108.65 399
2017-12-22T00:53	'LaLuz'	240	58 109.54 230
2017-12-23T00:54	'LaLuz'	127	58 110.54 298
2017-12-24T01:22	'LaLuz'	240	58 111.56 198
2017-12-25T01:26	'LaLuz'	242	58 112.56 500
2017-12-30T19:20	Rozhen	1200	58 118.31 067
2018-01-01T17:23	Rozhen	1200	58 120.22 886
2018-01-04T01:28	'LaLuz'	900	58 122.56 566
2018-01-04T03:56	'LaLuz'	900	58 122.66 813
2018-01-04T06:17	'LaLuz'	900	58 122.76 651
2018-01-05T01:21	'LaLuz'	900	58 123.56 049
2018-01-06T01:59	'LaLuz'	900	58 124.58 737
2018-01-06T04:19	'LaLuz'	900	58 124.68 461
2018-01-06T06:39	'LaLuz'	300	58 124.78 160
2018-01-07T01:23	'LaLuz'	900	58 125.56 225
2018-01-07T03:49	'LaLuz'	900	58 125.66 353
2018-01-07T06:14	'LaLuz'	900	58 125.76 423
2018-01-26T17:09	Rozhen	120	58 145.21 745
2018-01-26T17:12	Rozhen	180	58 145.21 951
2018-01-26T17:16	Rozhen	900	58 145.22 261
2018-01-26T17:32	Rozhen	1200	58 145.23 371
2018-02-01T17:09	Rozhen	1200	58 151.21 687
2018-02-01T17:30	Rozhen	300	58 151.23 149
2018-04-02T18:42	Rozhen	600	58 211.27 615
2018-04-02T18:53	Rozhen	120	58 211.28 358
2018-07-20T11:09	'LaLuz'	600	58 319.96 179
2018-08-02T11:20	'LaLuz'	600	58 332.97 006
2018-08-18T10:06	'LaLuz'	600	58 348.92 028
2018-08-19T01:10	Rozhen	120	58 349.54 794
2018-08-19T01:14	Rozhen	900	58 349.55 114
2018-08-30T00:11	Rozhen	600	58 360.50 863
2018-08-30T00:23	Rozhen	120	58 360.51 631
2018-08-31T01:50	Rozhen	600	58 361.57 747
2018-08-31T02:01	Rozhen	120	58 361.58 508
2018-09-01T01:13	Rozhen	600	58 362.55 181
2018-09-01T01:25	Rozhen	120	58 362.55 977
2018-09-02T02:39	Rozhen	600	58 363.61 129

Table A1 – *continued*

Date-obs	Obs.	Exp-time (s)	JD
2018-09-02T02:50	Rozhen	120	58 363.61 871
2018-09-03T01:21	Rozhen	600	58 364.55 719
2018-09-03T01:31	Rozhen	120	58 364.56 449
2018-09-05T08:54	'LaLuz'	600	58 366.87 215
2018-09-25T08:49	'LaLuz'	600	58 386.87 070
2018-10-10T07:16	'LaLuz'	600	58 401.80 672
2018-11-24T06:04	'LaLuz'	600	58 446.75 842
2018-11-25T22:30	Rozhen	180	58 448.44 317
2018-12-06T07:11	'LaLuz'	900	58 458.80 544
2018-12-18T07:07	'LaLuz'	900	58 470.80 209
2018-12-20T20:54	Rozhen	120	58 473.37 615
2018-12-20T20:57	Rozhen	900	58 473.37 847
2018-12-21T18:18	Rozhen	120	58 474.26 792
2018-12-21T18:21	Rozhen	900	58 474.26 989
2018-12-27T22:31	Rozhen	600	58 480.44 336
2018-12-27T22:42	Rozhen	120	58 480.45 117
2018-12-30T07:12	'LaLuz'	900	58 482.80 473
2019-01-11T07:14	'LaLuz'	900	58 494.80 544
2019-01-18T20:16	Rozhen	60	58 502.34 774
2019-01-18T20:19	Rozhen	120	58 502.34 988
2019-01-18T20:23	Rozhen	720	58 502.35 273
2019-01-18T20:37	Rozhen	900	58 502.36 252
2019-01-24T01:12	'LaLuz'	900	58 507.55 335
2019-02-07T01:37	'LaLuz'	900	58 521.56 939
2019-02-20T16:41	Rozhen	900	58 535.19 549
2019-02-20T16:57	Rozhen	120	58 535.20 681
2019-02-21T17:38	Rozhen	1200	58 536.23 481
2019-02-21T17:58	Rozhen	120	58 536.24 923
2019-03-02T01:51	'LaLuz'	1125	58 544.57 689
2019-03-17T18:50	Rozhen	600	58 560.28 307
2019-03-17T19:02	Rozhen	120	58 560.29 132
2019-03-23T19:10	Rozhen	120	58 566.29 626
2019-03-23T19:14	Rozhen	900	58 566.29 891
2019-03-25T18:19	Rozhen	120	58 568.26 056
2019-03-25T18:22	Rozhen	900	58 568.26 288
2019-07-18T00:30	Rozhen	600	58 682.51 763
2019-07-18T00:41	Rozhen	120	58 682.52 516
2019-07-19T00:51	Rozhen	600	58 683.53 222
2019-07-19T01:01	Rozhen	120	58 683.53 957
2019-08-19T00:43	Rozhen	600	58 714.52 967
2019-08-19T00:54	Rozhen	1200	58 714.53 737
2019-08-22T23:06	Rozhen	600	58 718.46 281
2019-08-22T23:18	Rozhen	120	58 718.47 082
2019-09-15T00:36	Rozhen	900	58 741.52 743
2019-09-15T00:53	Rozhen	120	58 741.53 915
2019-11-15T22:43	Rozhen	900	58 803.45 246
2019-11-15T22:43	Rozhen	900	58 803.45 246
2019-12-05T20:30	Rozhen	600	58 823.35 991
2019-12-05T20:41	Rozhen	120	58 823.36 759
2019-12-06T19:02	Rozhen	600	58 824.29 886
2019-12-06T19:13	Rozhen	120	58 824.30 628
2020-01-03T17:55	Rozhen	600	58 852.25 124
2020-01-03T18:06	Rozhen	120	58 852.25 892
2020-01-07T16:51	Rozhen	1200	58 856.20 631
2020-01-07T17:12	Rozhen	3600	58 856.22 133
2020-01-10T17:17	Rozhen	120	58 859.22 428
2020-01-10T17:23	Rozhen	900	58 859.22 862
2020-01-16T19:51	Rozhen	900	58 865.33 101
2020-01-16T20:08	Rozhen	120	58 865.34 259

Note. This table shows the date of observation, observatory, exposure time, and Julian Day (244 00000+).

Table A2. Parameters of the H α emission line.

JD	$W\alpha$	I_B	I_R	ΔV (km s^{-1})	V (km s^{-1})	V (km s^{-1})
58 095.21 084	−24.96	5.530	5.547	119.8	− 72.3	48.2
58 095.21 523	−24.09	5.316	5.252	121.0	− 72.9	48.0
58 095.22 714	−23.61	5.365	5.316	119.7	− 72.7	47.7
58 096.20 296	−24.43	5.581	5.598	119.0	− 72.7	47.6
58 096.20 597	−24.22	5.521	5.422	121.6	− 73.3	49.3
58 118.31 064	−22.61	4.954	5.006	123.7	− 77.5	45.9
58 120.22 892	−20.32	4.839	4.875	120.8	− 76.0	44.0
58 145.21 851	−18.61	4.162	4.709	108.0	− 74.5	33.5
58 145.22 057	−18.67	4.146	4.755	108.4	− 77.0	33.9
58 145.22 368	−18.25	4.141	4.741	110.3	− 76.5	33.7
58 145.23 478	−18.55	4.146	4.619	109.6	− 76.2	33.1
58 151.21 816	−18.77	4.076	4.859	116.2	− 85.1	32.5
58 151.23 277	−17.68	4.068	4.881	116.1	− 82.5	32.3
58 211.27 855	−16.35	3.519	4.480	106.6	− 89.0	17.6
58 211.28 598	−15.92	3.628	4.511	102.4	− 86.8	17.9
58 349.54 619	−18.81	3.440	5.197	105.3	− 98.0	12.4
58 349.54 938	−17.66	3.409	5.159	98.0	− 98.7	10.3
58 360.50 660	−18.42	3.278	5.383	100.7	− 93.8	9.2
58 360.51 428	−18.84	3.309	5.345	105.8	− 96.8	10.8
58 361.57 541	−17.77	3.139	5.173	97.8	− 90.0	3.2
58 361.58 303	−18.42	3.158	5.258	87.9	− 89.5	2.9
58 362.54 974	−18.92	3.247	5.363	94.8	− 89.0	5.3
58 362.55 770	−18.49	3.245	5.343	100.8	− 92.8	3.9
58 363.60 919	−19.45	3.292	5.438	98.5	− 94.8	1.5
58 363.61 661	−18.86	3.284	5.417	95.2	− 93.8	2.5
58 364.55 507	−18.88	3.304	5.386	95.2	− 96.9	2.9
58 364.56 238	−19.03	3.293	5.419	99.9	− 93.5	0.8
58 448.44 176	−21.17	3.371	5.767	115.9	− 115.0	2.1
58 473.37 570	−19.99	3.663	5.509	108.2	− 103.3	7.7
58 473.37 802	−20.87	3.607	5.397	115.2	− 106.1	6.3
58 474.26 750	−20.30	3.606	5.448	110.6	− 101.9	9.2
58 474.26 947	−20.24	3.507	5.400	112.9	− 105.6	5.8
58 480.44 321	−21.40	3.710	5.538	112.0	− 106.1	8.1
58 480.45 101	−21.28	3.802	5.691	110.4	− 106.5	8.8
58 502.34 850	−20.51	3.822	5.251	105.8	− 99.7	11.6
58 502.35 064	−20.05	3.836	5.252	109.7	− 104.7	12.1
58 502.35 348	−20.54	3.809	5.196	109.3	− 103.1	12.0
58 502.36 328	−20.25	3.833	5.222	112.0	− 102.5	11.7
58 535.19 736	−19.42	3.714	5.307	114.6	− 94.8	21.8
58 535.20 868	−20.20	3.747	5.353	115.9	− 94.4	20.4
58 536.23 671	−20.01	3.678	5.219	116.5	− 97.8	21.7
58 536.25 113	−19.68	3.743	5.286	117.6	− 98.7	20.8
58 560.28 540	−20.20	3.905	4.708	108.3	− 87.3	21.9
58 560.29 365	−19.43	3.893	4.837	106.9	− 85.9	21.0
58 566.29 864	−21.40	4.367	4.845	108.3	− 87.6	26.7
58 566.30 129	−20.18	4.117	4.788	110.6	− 86.3	25.8
58 568.26 295	−19.94	4.175	4.693	107.3	− 82.3	25.3
58 568.26 527	−20.45	4.093	4.686	108.3	− 81.8	25.4
58 108.65 545	−23.37	5.518	5.257	125.3	− 69.8	56.3
58 109.54 377	−23.51	5.421	5.273	121.6	− 66.1	58.4
58 110.54 374	−24.88	5.477	5.217	123.8	− 69.0	55.1
58 111.56 345	−26.02	5.385	5.244	125.2	− 72.0	50.6
58 112.56 647	−23.20	5.046	5.056	123.9	− 65.5	57.3
58 122.57 100	−20.95	4.840	4.850	124.3	− 72.3	51.6
58 122.67 347	−21.42	4.890	4.931	123.4	− 73.8	50.4
58 122.77 185	−21.03	4.859	4.884	124.6	− 74.0	50.4
58 123.56 58 2	−22.24	5.003	5.008	125.2	− 72.7	51.3
58 124.59 271	−22.08	4.983	4.921	122.4	− 74.1	49.0
58 124.68 994	−20.87	4.933	4.892	122.4	− 74.8	47.8
58 124.78 338	−20.99	4.921	4.856	122.6	− 75.1	48.5
58 125.56 759	−20.60	4.849	4.829	123.2	− 72.0	50.9
58 125.66 887	−20.71	4.888	4.872	122.0	− 72.9	49.2
58 125.76 956	−21.29	4.902	4.887	122.2	− 73.7	49.6
58 319.96 541	−16.63	3.143	4.770	107.5	− 95.4	18.2
58 332.97 367	−16.86	3.144	5.053	107.9	− 96.7	16.2
58 348.92 388	−19.44	3.499	5.272	100.4	− 96.5	12.7
58 366.87 575	−20.47	3.436	5.451	100.3	− 93.3	12.4
58 386.87 432	−20.88	3.508	5.680	98.9	− 102.3	6.1
58 401.81 034	−21.58	3.908	5.515	100.3	− 96.5	8.1
58 446.76 209	−20.95	3.400	5.717	120.5	− 112.6	8.3
58 458.81 081	−19.76	3.172	5.571	117.9	− 116.1	12.3
58 470.80 746	−20.75	3.496	5.368	114.9	− 108.5	13.3
58 482.81 011	−20.85	3.744	5.403	105.9	− 99.0	10.7
58 494.81 083	−21.35	3.815	5.372	90.4	− 85.8	10.6
58 507.55 8 74	−20.20	3.730	5.266	102.4	− 95.2	16.5
58 521.57 478	−20.01	3.636	5.246	116.7	− 98.1	20.6
58 544.58 365	−20.18	3.939	5.038	109.6	− 84.3	31.4
58 682.52 460	−16.63	4.196	3.755	110.5	− 82.3	26.0
58 682.52 940	−17.08	–	–	–	–	–
58 683.53 920	−17.11	4.182	3.864	112.7	− 83.0	24.2
58 683.54 370	−16.64	4.261	3.931	109.1	− 73.7	21.7
58 714.53 390	−15.77	3.998	3.579	103.3	− 75.1	25.5
58 714.54 510	−15.39	4.002	3.633	108.1	− 75.1	28.5
58 718.46 660	−15.81	3.925	3.686	110.3	− 75.6	34.2
58 718.47 190	−15.64	3.951	3.740	110.3	− 76.4	36.0
58 741.53 080	−14.26	4.135	3.377	106.1	− 68.5	34.3
58 741.53 800	−14.31	4.158	3.432	102.1	− 67.5	28.7
58 803.45 210	−12.39	3.829	2.898	112.9	− 55.4	57.2
58 803.45 210	−12.49	3.835	2.916	111.1	− 55.7	56.4
58 823.35 790	−11.58	3.637	2.550	107.7	− 50.6	59.7
58 823.36 280	−11.03	3.625	2.548	110.5	− 49.6	63.9
58 824.29 680	−11.66	3.621	2.482	109.1	− 55.1	58.6
58 824.30 150	−10.92	3.618	2.481	113.3	− 55.8	59.7
58 852.25 040	−10.15	3.294	2.374	119.2	− 58.2	56.4
58 852.25 530	−10.26	3.339	2.398	114.4	− 58.1	58.1
58 856.20 920	−10.51	3.251	2.395	106.8	− 56.3	54.8
58 856.23 810	−10.32	3.179	2.347	110.5	− 58.6	55.1
58 859.22 110	−10.33	3.176	2.372	125.3	− 58.7	67.4
58 859.23 000	−10.06	3.153	2.362	127.7	− 58.8	65.6
58 865.33 290	−10.20	3.161	2.370	120.8	− 59.7	63.1
58 865.33 990	−10.19	3.231	2.414	119.4	− 60.4	62.9

Table A2 – *continued*

Note. This table shows Julian Day (2400 000+), equivalent width, intensity of the violet and red peaks, distance between the peaks, and radial velocities of the peaks.

Table A3. Parameters of the H β emission line.

58 095.21 084	−4.357	2.094	2.167	150.5	− 87.3	61.7	–
58 095.21 523	−4.140	2.092	2.115	150.9	− 86.5	64.2	–
58 095.22 714	−4.172	2.088	2.116	151.0	− 87.3	63.9	–
58 096.20 296	−4.132	2.161	2.131	148.9	− 85.8	63.3	–
58 096.20 597	−4.184	2.122	2.115	148.8	− 88.1	61.7	–
58 118.31 064	−3.699	1.965	2.094	148.1	− 91.9	58.7	–
58 120.22 892	−3.814	1.944	2.106	143.9	− 87.9	56.7	–
58 145.21 851	−3.262	1.775	2.039	141.5	− 78.7	65.7	–
58 145.22 057	−3.315	1.763	2.048	137.0	− 78.1	62.8	–
58 145.22 368	−3.322	1.754	2.015	140.1	− 78.9	63.3	–
58 145.23 478	−3.360	1.762	2.023	140.3	− 80.2	62.5	–
58 151.21 816	−3.259	1.725	2.074	138.0	− 102.0	40.0	–
58 151.23 277	−3.509	1.747	2.088	141.8	− 107.1	40.0	–
58 211.27 855	−2.544	1.548	1.918	106.5	− 84.4	28.8	–
58 211.28 598	−2.683	1.545	1.936	127.6	− 97.2	28.0	–
58 349.54 619	−3.123	1.520	2.095	125.0	− 119.1	19.3	–
58 349.54 938	−3.150	1.505	2.018	130.0	− 113.1	21.7	–
58 360.50 660	−2.963	1.449	2.035	132.7	− 120.0	19.6	–
58 360.51 428	−3.062	1.469	2.059	131.5	− 115.7	18.7	–
58 361.57 541	−3.034	1.413	2.021	131.2	− 116.9	19.6	–
58 361.58 303	−3.096	1.437	2.040	135.7	− 111.8	20.4	–
58 362.54 974	−2.815	1.439	2.072	137.4	− 116.8	17.9	–
58 362.55 770	−3.151	1.447	2.062	139.1	− 124.8	19.3	–
58 363.60 919	−3.133	1.434	2.066	140.0	− 121.7	18.4	–
58 363.61 661	−2.993	1.437	2.068	130.8	− 117.9	16.0	–
58 364.55 507	−3.103	1.460	2.038	141.3	− 155.3	− 18.6	–
58 364.56 238	−3.072	1.475	2.023	144.1	− 153.9	− 16.1	–

Table A3 – *continued*

58 448.44 176	−3.263	1.552	2.021	163.8	− 155.9	10.1	–
58 473.37 570	−3.328	1.576	2.012	147.7	− 122.6	25.2	–
58 473.37 802	−3.450	1.548	1.985	147.8	− 123.4	22.2	–
58 474.26 750	−3.288	1.535	2.106	158.2	− 130.1	25.0	–
58 474.26 947	−3.219	1.515	2.010	148.9	− 124.8	23.5	–
58 480.44 321	−3.179	1.549	2.005	153.6	− 127.9	21.5	–
58 480.45 101	−3.078	1.549	2.026	148.9	− 126.9	20.6	–
58 502.34 850	−3.392	1.597	1.933	145.1	− 99.0	40.1	–
58 502.35 064	−3.229	1.590	1.910	150.2	− 107.6	39.4	–
58 502.35 348	−3.347	1.601	1.932	149.4	− 108.9	41.1	–
58 502.36 328	−3.307	1.588	1.923	152.4	− 109.7	40.1	–
58 535.19 736	−3.198	1.569	1.866	150.0	− 122.2	27.5	–
58 535.20 868	−3.131	1.590	1.941	152.8	− 125.8	26.1	–
58 536.23 671	−2.858	1.574	1.875	158.9	− 128.8	29.1	–
58 536.25 113	−2.988	1.601	1.897	161.1	− 127.4	29.4	–
58 560.28 540	−2.870	1.629	1.726	147.6	− 118.7	29.5	–
58 560.29 365	−2.885	1.661	1.739	145.0	− 118.6	27.7	–
58 566.29 864	−3.198	1.772	1.809	146.9	− 117.2	28.4	–
58 566.30 129	−2.738	1.672	1.691	–	–	–	–
58 568.26 295	−2.934	1.706	1.732	148.7	− 115.8	25.1	–
58 568.26 527	−3.073	1.698	1.707	146.0	− 115.5	30.4	–
58 108.65 545	−4.003	1.969	2.157	152.7	− 84.4	68.1	–
58 109.54 377	−3.924	1.971	2.126	145.7	− 83.1	62.5	–
58 110.54 374	−4.017	2.109	2.273	145.2	–	–	–
58 111.56 345	−4.062	1.999	2.206	149.0	− 88.7	63.9	–
58 112.56 647	−3.892	2.006	2.168	147.0	− 84.4	63.1	–
58 122.57 100	−3.621	1.835	2.059	148.4	− 94.9	58.0	–
58 122.67 347	−3.521	1.892	2.053	149.8	− 91.5	56.0	–
58 122.77 185	−3.525	1.845	2.039	150.0	− 94.5	57.7	–
58 123.56 58 2	−3.613	1.880	2.062	148.7	− 90.5	57.6	–
58 124.59 271	−3.615	1.899	2.066	146.3	− 87.6	58.1	–
58 124.68 994	−3.488	1.868	2.023	145.8	− 89.9	54.9	–
58 124.78 338	−3.548	1.855	2.047	143.8	− 86.6	55.0	–
58 125.56 759	−3.582	1.871	2.059	140.7	− 89.7	53.3	–
58 125.66 887	−3.569	1.917	2.035	142.8	− 89.2	54.6	–
58 125.76 956	−3.541	1.859	2.021	143.0	− 88.7	55.5	–
58 319.96 541	−2.779	1.442	1.966	120.2	− 97.5	26.2	–
58 332.97 367	−2.733	1.450	1.980	126.0	–	–	–
58 348.92 388	−2.979	1.536	2.031	127.2	− 106.0	21.4	–
58 366.87 575	−3.002	1.505	2.076	124.7	− 106.5	18.9	–
58 386.87 432	−3.309	1.474	2.056	144.2	− 130.4	18.4	–
58 401.81 034	−3.424	1.598	2.047	139.0	− 124.3	17.0	–
58 446.76 209	−3.257	1.578	2.034	166.9	− 152.5	16.2	–
58 458.81 081	−3.001	1.509	2.006	167.5	− 147.9	20.1	–
58 470.80 746	−3.126	1.541	1.964	152.3	− 128.5	23.2	–
58 482.81 011	−3.067	1.556	1.911	141.6	− 121.9	21.7	–
58 494.81 083	−3.104	1.523	1.956	146.7	− 126.4	21.1	–
58 507.55 8 74	−3.032	1.565	1.852	156.7	− 127.8	27.3	–
58 521.57 478	−2.855	1.567	1.842	157.9	− 132.4	27.8	–
58 544.58 365	−2.764	1.584	1.773	155.7	− 114.4	38.8	–
58 682.52 460	−2.246	1.630	1.400	117.1	− 98.3	23.3	220.0
58 682.52 940	–	–	–	–	–	–	–
58 683.53 920	−2.309	1.598	1.377	113.2	− 100.5	23.8	206.6
58 683.54 370	−2.355	1.604	1.400	109.8	− 100.4	17.1	196.9
58 714.53 390	−2.100	1.619	1.357	123.3	− 90.8	24.9	202.2
58 714.54 510	−2.015	1.603	1.358	119.9	− 91.5	31.5	197.5
58 718.46 660	−2.039	1.608	1.389	122.0	− 89.8	34.2	197.7
58 718.47 190	−2.009	1.598	1.433	122.2	− 89.7	31.0	191.5
58 741.53 080	−1.896	1.615	1.315	125.3	− 81.0	47.2	207.0
58 741.53 800	−2.019	1.661	1.324	141.8	− 81.2	24.8	194.1
58 803.45 210	−1.675	1.536	1.261	131.4	− 70.8	65.4	170.1
58 803.46 410	−1.594	1.518	1.248	130.0	− 70.2	61.8	163.1
58 823.35 790	−1.571	1.502	1.215	128.1	− 65.7	65.9	162.5
58 823.36 280	−1.628	1.509	1.251	126.2	− 65.4	63.7	166.7
58 824.29 680	−1.456	1.497	1.202	128.7	− 68.7	65.2	153.4
58 824.30 150	−1.507	1.479	1.224	127.3	− 68.8	60.1	151.3
58 852.25 040	−1.438	1.439	1.119	149.0	− 68.7	89.0	–
58 852.25 530	−1.473	1.467	1.225	148.9	− 69.1	96.8	–
58 856.20 920	−1.498	1.415	1.242	155.8	− 67.9	88.3	–

Table A3 – *continued*

58 856.23 810	−1.481	1.429	1.221	147.2	− 68.4	86.5	–
58 859.22 110	−1.475	1.422	1.224	152.3	− 68.7	89.3	–
58 859.23 000	−1.427	1.421	1.210	148.7	− 68.6	78.7	–
58 865.33 290	−1.427	1.434	1.244	173.3	− 67.6	96.1	–
58 865.33 990	−1.366	1.431	1.259	165.5	− 69.4	87.3	–

Note. This table shows Julian Day (2400 000+), equivalent width, intensity of the violet and red peaks, and distance between the peaks.

Table A4. Parameters of the He I 6678 emission line.

JD	$W\alpha$	I_B	I_R	ΔV (km s^{-1})	V (km s^{-1})	V (km s^{-1})	V (km s^{-1})
58 095.21 084	−2.004	1.363	1.346	181.9	−98.0	81.7	
58 095.21 523	−1.908	1.334	1.323	182.5	−95.5	84.2	
58 095.22 714	−1.917	1.327	1.325	178.9	−100.2	82.7	
58 096.20 296	−2.030	1.344	1.363	178.3	−101.0	81.0	
58 096.20 597	−1.973	1.340	1.330	179.3	−98.3	84.8	
58 118.31 064	−1.564	1.278	1.301	180.9	−111.3	71.2	
58 120.22 892	−1.470	1.264	1.272	169.3	−102.8	67.8	
58 145.21 851	−1.118	1.185	1.240	159.1	−105.6	52.8	
58 145.22 057	−1.229	1.179	1.251	154.6	−99.8	53.6	
58 145.22 368	−1.193	1.174	1.246	155.1	−106.6	53.1	
58 145.23 478	−1.202	1.183	1.242	164.2	−111.5	54.2	
58 151.21 816	−1.180	1.178	1.263	165.3	−116.1	49.5	
58 151.23 277	−1.073	1.193	1.271	168.0	−115.8	52.8	
58 211.27 855	−0.865	1.107	1.206	166.8	−127.2	43.1	
58 211.28 598	−0.922	1.114	1.209	–	–	–	
58 349.54 619	−0.904	1.110	1.210	201.8	−164.5	34.3	
58 349.54 938	−0.816	1.100	1.195	202.8	−169.8	35.3	
58 360.50 660	−0.932	1.109	1.196	212.0	−181.8	29.9	
58 360.51 428	−0.907	1.113	1.209	190.3	−165.4	26.0	
58 361.57 541	−0.939	1.109	1.212	211.7	−185.9	29.1	
58 361.58 303	−0.911	1.106	1.218	200.5	−173.1	28.8	
58 362.54 974	−0.927	1.095	1.214	201.2	−167.9	30.2	
58 362.55 770	−0.950	1.103	1.205	196.0	−161.1	31.5	
58 363.60 919	−1.044	1.099	1.219	209.0	−179.9	29.8	
58 363.61 661	−1.089	1.107	1.231	204.9	−172.4	29.9	
58 364.55 507	−1.112	1.107	1.200	209.7	−173.5	28.8	
58 364.56 238	−1.104	1.121	1.205	201.8	−172.6	30.6	
58 448.44 176	−1.586	1.197	1.243	206.9	−182.7	25.4	
58 473.37 570	−1.749	1.201	1.244	217.6	−189.1	32.5	
58 473.37 802	−1.665	1.178	1.210	211.5	−188.1	27.2	199.1
58 474.26 750	−1.540	1.218	1.262	212.2	−185.4	25.3	–
58 474.26 947	−1.573	1.186	1.212	218.3	−190.9	26.5	187.0
58 480.44 321	−1.653	1.214	1.227	218.8	−190.9	28.0	163.3
58 480.45 101	−1.942	1.265	1.297	205.2	−185.5	26.1	–
58 502.34 850	−1.550	1.233	1.216	199.9	−176.6	22.1	–
58 502.35 064	−1.580	1.208	1.194	201.7	−171.3	28.6	–
58 502.35 348	−1.475	1.212	1.197	198.4	−166.7	28.0	205.8
58 502.36 328	−1.591	1.211	1.193	201.7	−172.5	27.5	206.8
58 535.19 736	−1.505	1.205	1.178	191.2	−157.2	32.2	231.0
58 535.20 868	−1.536	1.217	1.195	192.6	−162.1	34.6	204.6
58 536.23 671	−1.505	1.205	1.171	180.2	−149.2	34.5	229.0
58 536.25 113	−1.522	1.221	1.183	185.4	−152.7	31.8	234.8
58 560.28 540	−1.427	1.216	1.138	177.4	−144.8	30.0	246.5
58 560.29 365	−1.520	1.232	1.130	176.2	−152.9	28.7	223.3
58 566.29 864	−1.648	1.242	1.175	−1.0	–	–	–
58 566.30 129	−1.470	1.220	1.141	160.2	−144.8	23.5	245.2
58 568.26 295	−1.486	1.229	1.159	141.9	−138.9	11.1	250.1
58 568.26 527	−1.375	1.224	1.142	162.2	−133.3	25.5	240.9
58 108.65 545	−1.501	1.233	1.312	180.5	−94.5	84.2	
58 109.54 377	−1.485	1.240	1.314	177.0	−87.3	87.2	
58 110.54 374	−1.417	1.246	1.316	174.6	−90.6	80.2	
58 111.56 345	−1.406	1.214	1.315	174.1	−92.9	80.1	
58 112.56 647	−1.417	1.247	1.332	181.2	−94.4	85.8	
58 122.57 100	−1.180	1.199	1.292	181.0	−105.4	75.1	
58 122.67 347	−1.165	1.197	1.280	183.2	−107.5	73.5	
58 122.77 185	−1.120	1.198	1.280	184.3	−105.2	75.2	

Table A4 – *continued*

JD	$W\alpha$	I_B	I_R	ΔV (km s^{-1})	V (km s^{-1})	V (km s^{-1})	V (km s^{-1})
58 123.56 582	−1.129	1.199	1.276	178.9	−100.1	76.1	
58 124.59 271	−1.115	1.198	1.265	173.3	−98.1	74.1	
58 124.68 994	−1.113	1.197	1.273	170.8	−98.3	73.4	
58 124.78 338	−1.134	1.200	1.281	172.2	−97.6	71.7	
58 125.56 759	−1.114	1.190	1.277	173.0	−97.2	74.3	
58 125.66 887	−1.176	1.190	1.281	175.5	−97.3	73.8	
58 125.76 956	−1.124	1.191	1.268	178.0	−99.8	73.1	
58 319.96 541	−0.687	1.074	1.149	209.9	−156.8	35.3	
58 332.97 367	−0.707	1.078	1.171	219.8	−182.9	37.3	
58 348.92 388	−0.857	1.105	1.186	210.5	−178.2	32.3	
58 366.87 575	−0.936	1.108	1.197	203.8	−176.2	35.9	
58 386.87 432	−1.162	1.141	1.198	233.5	−204.5	35.7	
58 401.81 034	−1.269	1.166	1.210	215.9	−184.4	36.9	
58 446.76 209	−1.383	1.207	1.197	217.8	−183.2	32.8	
58 458.81 081	−1.319	1.159	1.193	223.6	−192.5	32.1	
58 470.80 746	−1.326	1.170	1.196	223.3	−185.8	35.0	
58 482.81 011	−1.475	1.196	1.204	211.6	−179.6	30.0	201.7
58 494.81 083	−1.394	1.187	1.202	201.5	−177.1	24.7	174.4
58 507.55 8 74	−1.454	1.218	1.171	206.1	−174.9	33.9	208.6
58 521.57 478	−1.381	1.188	1.167	196.6	−167.8	28.4	217.5
58 544.58 365	−1.351	1.206	1.167	179.0	−142.5	36.9	232.3
58 682.52 460	−0.896	1.223	1.089	367.4	−117.1	242.3	
58 683.53 920	−0.873	1.229	1.081	357.9	−120.7	235.8	
58 683.54 370	−0.817	1.228	1.106	358.4	−116.9	244.8	

Table A4 – *continued*

JD	$W\alpha$	I_B	I_R	ΔV (km s^{-1})	V (km s^{-1})	V (km s^{-1})	V (km s^{-1})
58 714.53 390	−0.813	1.180	1.088	348.2	−104.4	242.5	
58 714.54 510	−0.781	1.176	1.083	353.4	−107.6	244.7	
58 718.46 660	−0.796	1.182	1.081	345.4	−104.5	239.8	
58 718.47 190	−0.808	1.192	1.104	341.3	−103.1	240.1	
58 741.53 080	−0.716	1.197	1.081	331.9	−95.1	240.6	
58 741.53 800	−0.727	1.191	1.091	335.8	−92.9	235.8	
58 803.45 210	−0.586	1.129	1.092	279.2	−72.6	208.5	
58 803.46 410	−0.570	1.120	1.091	271.5	−72.6	201.9	
58 823.35 790	−0.510	1.115	1.080	257.3	−67.3	195.5	
58 823.36 280	−0.518	1.122	1.091	260.1	−67.6	197.3	
58 824.29 680	−0.521	1.118	1.092	263.3	−73.2	192.4	
58 824.30 150	−0.494	1.121	1.094	267.6	−74.4	192.9	
58 852.25 040	−0.436	1.110	1.069	244.1	−67.8	179.2	
58 852.25 530	−0.446	1.118	1.079	254.5	−68.4	179.4	
58 856.20 920	−0.422	1.107	1.081	225.4	−67.6	160.1	
58 856.23 810	−0.413	1.088	1.087	231.4	−67.2	163.2	
58 859.22 110	−0.401	–	–	–	–	–	
58 859.23 000	−0.417	1.098	1.073	223.4	−70.8	152.7	
58 865.33 290	−0.417	1.086	1.078	216.4	−64.9	150.5	

Note. This table shows Julian Day (2400 000+), equivalent width, intensity of the violet and red peaks, distance between the peaks, and the radial velocities of the peaks.

This paper has been typeset from a TEX/LATEX file prepared by the author.